ACS APPLIED ENERGY MATERIALS
Cite This: ACS Appl. Energy Mater. 2018, 1, 3984−3991
Article
www.acsaem.org

General Method To Define the Type of Carrier Transport Materials for Perovskite Solar Cells via Kelvin Probes Microscopy

Yinghui Wu,[†,‡,∥] Wei Chen,[†,§,∥] Yi Lin,[†] Bao Tu,[†] Xiaoqi Lan,[†] Zhenggang Wu,[†] Ruchuan Liu,[*,‡] Aleksandra B. Djurišić,[§] and Zhu Bing He[*,†]

[†]Department of Materials Science and Engineering, Shenzhen Key Laboratory of Full Spectral Solar Electricity Generation (FSSEG), Southern University of Science and Technology, No.1088, Xueyuan Road, Shenzhen 518055, Guangdong, China

[‡]Department of Physics, Chongqing University, No.55, University City South Road, Chongqing 401331, China

[§]Department of Physics, The University of Hong Kong, Pokfulam, Hong Kong SAR, China

Supporting Information

ABSTRACT: Various kinds of semiconductor materials, organic and inorganic, served effectively as electrons or holes transport materials for perovskite solar cells (PSCs). However, their direct function has rarely been reported other than examining their effect in the final photovoltaic devices. In this work, a general and facile method was employed to determine to a point the type of carriers transferred by both SnO_2 and NiO popular charge transport materials in PSCs via scanning Kelvin probes microscopy. The sign of the increment of the surface potential voltage measured tells directly whether electrons or holes were extracted by these carrier transport materials while its mapping can also provide the extraction difference between grain interiors and grain boundaries. Both $MAPbI_3$ and CsFAMA triple cation perovskites were involved in the test with the same conclusion. Along with time-resolved photoluminescence, the extraction rate of each kind of material can be distinguished. This work definitely offers us a general and effective method to distinguish the carrier transport ability of either electrons or holes transport materials with indisputable clarification of carrier types and further to screen out optimal carrier transport materials for perovskite solar cells and more.

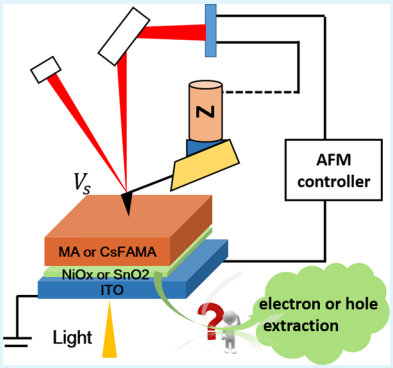

KEYWORDS: *carriers transport materials, charge transfer, SnO_2, NiO, scanning Kelvin probes microscopy (SKPM)*

INTRODUCTION

Lead halide perovskites show huge potential in photovoltaics, with excitingly over 20% in power conversion efficiency (PCE) and a certified world record of PCE, 22.7%, surpassing that of polycrystalline silicon, cadmium telluride, and copper−indium−gallium−selenide series.[1−4] In any device structures of perovskite solar cells (PSCs), the extraction ability of both holes and electrons transport layers sandwiched with a perovskites layer predominates the device performance. Various protocols, such as photoluminescence (PL) decay, electrochemical impedance spectroscopy, transient absorption and reflection, transient photovoltage and photocurrent, scanning probe microscopy, and other techniques were extensively applied to discover the charge transfer process.[5−9] Different from those mentioned, scanning Kelvin probes microscopy (SKPM) can directly image the real time charge transport with high spatial resolution.[10,11] In situ observation of interface charge transfer across the cross-section of devices was successfully obtained by SKPM with or without light illumination, which revealed that the extraction rate of electrons by TiO_2 is much faster than that of HTM[12−15] and it probably results in the hysteresis in $I−V$ curves of devices.[16−19] In contrast to measurement of cross-section potential distribution in complete devices, more facile topographical SKPM was conducted popularly to investigate charge transfer between perovskite and its underlayers.[10,13,20,21] Through detecting contact potential difference in the dark and under illumination, it was discovered that grain boundaries, grain size, and compactness facilitate photogenerated electrons transfer from perovskite to its underlying layer.[15,22−26] By a fast SKPM, a series of real-time nanoscale potential images distinguished the dynamic variation in open-circuit voltage of grains and grain boundaries and discovered illumination can drive the equilibrium of moving ions in perovskites.[27]

Among those reports mentioned above, it is really rare to investigate a basic function of charge type of carriers' transport layers in devices by SKPM. Assisted by time-resolved PL, this function is so important to screen out optimal carrier transport materials from versatile candidates for sustainable technique development of PSCs. Meanwhile, extensive efforts were devoted to enhance carrier transfer at both anode and cathode sides by use of band-level tunable and stable metal oxides with suitable valence band maximum (VBM) or conduction band

Received: April 27, 2018
Accepted: July 20, 2018
Published: July 20, 2018

DOI: 10.1021/acsaem.8b00687
ACS Appl. Energy Mater. 2018, 1, 3984−3991

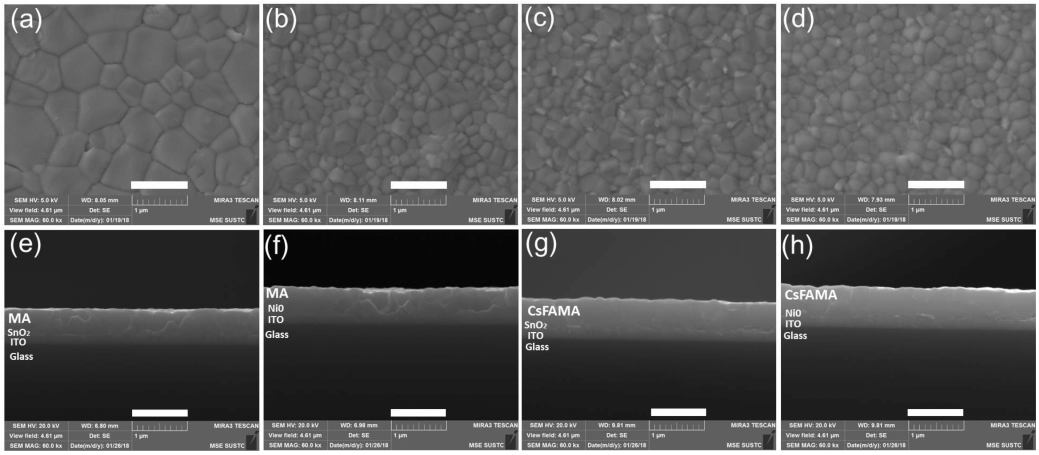

Figure 1. Topographic SEM images of MA perovskite films on SnO_2/ITO glass (a) and on NiO/ITO glass (b); CsFAMA triple cations perovskite films on SnO_2/ITO glass (c) and on NiO/ITO glass (d); cross-section SEM images of MA perovskite films on SnO_2/ITO glass (e) and on NiO/ITO glass (f); CsFAMA triple cations perovskite films on SnO_2/ITO glass (g) and on NiO/ITO glass (h). The scale bar is 1 μm for all images.

minimum (CBM) matching that of perovskites.[28−30] Among them, NiO[31−35] has become one of the most promising candidates for holes extraction especially in the planar inverted PSCs while SnO_2[36−41] acts in an efficient electron extraction role in the normal planar device structures. So, it is of particular interest to verify kinds and rates of charge extraction by NiO and SnO_2 in each corresponding device structure by function of SKPM and PL.

In this work, a light illumination coupled SKPM system was applied in brief to examine electrons or holes extraction behavior by two popular carrier transport materials, SnO_2 and NiO. Both $MAPbI_3$ and mixed cations perovskite materials were involved in a series of tests to testify to the extraction effect of them. Along with PL and time-resolved PL, the extraction rates of them were also distinguished besides the carriers type.

EXPERIMENTAL SECTION

All solvents including anhydrous dimenthylformamide (DMF) and dimethyl sulfoxide (DMSO) were purchased from Acros Organic and Sigma-Aldrich and used without additional processing. Nickel(II) nitrate hexahydrate (99.998%) was obtained from Alfa Aesar and used as received. The SnO_2 colloid precursor was purchased from Alfa Aesar (tin(IV) oxide, 15% aqueous colloidal dispersion). Lead(II) iodide (99.99%) and lead(II) bromide were obtained from TCI. Methanaminium iodide (MAI), methanaminium bromide (MABr), and formamidine iodide (FAI) were purchased from Greatcell Solar Ltd. (Australia).

NiO nanoparticles were synthesized according to our previous reports.[42] Briefly, nickel(II) nitrate hexahydrate (9 g) was dissolved in 120 mL of deionized (DI) water and stirred at room temperature to obtain a clear green solution, and then 1.5 M sodium hydroxide solutions were added to tune its pH value. After 10 min of stirring, the green educts were collected by centrifugation and washed by DI water three times. The obtained green powders were dried at 80 °C for 8 h and calcined for 2 h at 275 °C. Finally, a dark gray powder was obtained. The NiO powder was dissolved in deionized water with a concentration of 2.67%.

The ITO glass substrates were cleaned in an ultrasonic bath using detergent, acetone, and isopropanol, respectively, for 20 min. Then, the ITO glass was exposed to UVO for 15 min. For NiO/ITO, 20 mg/mL NiO nanoparticles were dissolved in DI water. The final solution was spin coated on cleaned ITO glass substrates at room temperature at 3,000 rpm for 30 s and then annealed on a hot plate in ambient air at 100 °C for 5 min. For SnO_2/ITO, a diluted SnO_2 precursor was spin coated on cleaned ITO glass substrates at room temperature at 3,000 rpm for 30 s and then annealed on a hot plate in ambient air at 170 °C for 30 min. After cooling to room temperature, the substrate coated with SnO_2 or NiO film was waiting for the coating of perovskite films.

For $MAPbI_3$ (MA) perovskite deposition, a precursor solution contains 160 mg of PbI_2 and 461 mg of CH_3NH_3I in a mixture solvent of DMF and DMSO (8:1 (v/v)). The precursor solution was then filtered using a 0.2 μm PTFE syringe filter and spin coated onto those SnO_2 (NiO) /ITO substrates with a speed of 3,500 rpm for 35 s and quenched by chlorobenzene in the first 15 s. The films were then annealed on a hot plate at 75 °C for 25 min and 100 °C for 15 min successively. For the CsFAMA mixed precursor solution, 1.02 M FAI, 0.18 M MABr, 1.105 M PbI_2, and 0.195 M $PbBr_2$ were dissolved in 1 mL of DMF/DMSO (4:1) mixed solvents and stirred at 65 °C for 1 h. CsI was separately dissolved (2 M stock solution in dimethyl sulfoxide) and added to the mixed perovskite precursor to achieve the desired composition (5%). The precursor solution was spin coated onto those SnO_2 (NiO) /ITO substrates with a speed of 2,000 rpm for 10 s and 6,000 rpm for 30 s and then annealed at 100 °C for 30 min.

X-ray diffraction (XRD) patterns were measured with a multifunction powder diffractometer (BRUKER ECO D8 1 KW). Photoluminescne (PL) measurements were performed by Horiba 320 spectrometer with a 300 lines/mm grating and collected with an InGaAs charged couped device (CCD) (Andor iDus),exciting the samples with a Coherent Sapphire SF 532 nm-150 CW laser. PL lifetime curves were measured by an Edinburgh FS5 fluorescence spectrometer equipped with a 405 nm paused laser. Absorption spectra were recorded by a UV/vis/near-IR spectrometer (LAMBDA 950, PerkinElmer) in the wavelength range of 550−800 nm. Top-view and cross-section scanning electron microscopy (SEM) images were characterized by TESCAN MIRA3 scanning electron microscope.

All atomic force microscopy (AFM) based experiments were performed in ambient condition using an MFP-3D-BIO AFM (Asylum Research, USA), and Ti/Ir coated silicon tips (ASYE-LELC-01-R2) with a spring constant of $k \sim 1.4-5.8$ N/m and a resonance frequency at ~58−97 kHz were used in scanning Kelvin probe microscopy (SKPM) imaging. The whole AFM system is integrated on top of an optical microscope (IX71, Olympus), so the sample can be easily illuminated through a 40× objective in the measurements. The light source is a focused, unfiltered BXRC-50C10K0-L LED (BRIDGELUX) with an approximate illumination intensity of 0.01 W cm^{-2} (equivalent to 0.1 sun but not AM1.5G spectrum) .

Scanning Kelvin probe microscopy measurements were conducted with one identical probe at 35% relative humidity (RH) and 25 °C within 1 day. The work functions of Ti/Ir alloy range from 5.0 and

DOI: 10.1021/acsaem.8b00687
ACS Appl. Energy Mater. 2018, 1, 3984−3991

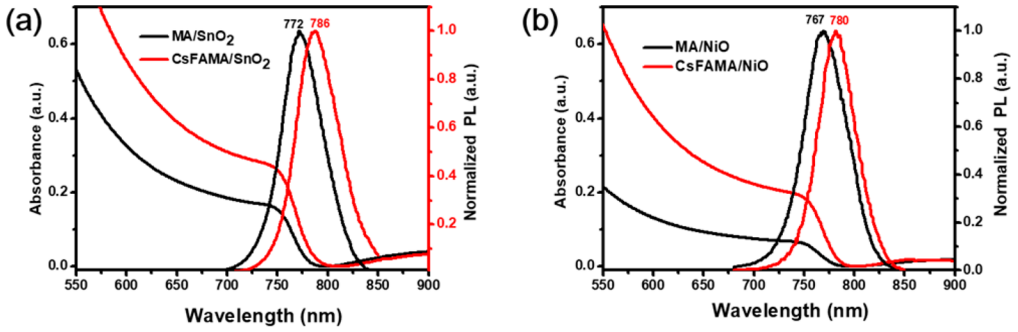

Figure 2. (a) Absorption and PL spectra of MA and CsFAMA films on SnO_2/ITO glass; (b) MA and CsFAMA films on NiO/ITO glass.

5.67 eV in air environment, which also claims it is difficult to identify a definite dividing span of surface potential voltages measured. The surface of the sample in the test was grounded. Amplitude modulation (AM-) SKPM was adopted in this work and carried out in a two-pass manner, which has a merit of decoupling the signal of topography and surface potential on orthogonal frequencies. The first pass is used to determine the topography of the surface while the return trace is to measure the surface potential after lifting the probe at a slight height (below 50 nm) above the measured sample surface of the first trace. In the second process, raising the tip away from the surface eliminates cross-talk between topography and surface potential, while the close distance between tip and surface enhances the lateral resolution of electrostatic forces, which is examined by our clear SKPM images in the following text. An AC voltage ($V_{AC}\sin(\omega t)$) signal is applied to induce a mechanical oscillation proportional to the tip−surface electrostatic interaction strength, while a dynamic bucking DC voltage (V_{DC}) added to the probe is in order to minimize the surface potential difference between tip and sample surface.

RESULTS AND DISSCUSSION

The SnO_2 ETLs and NiO HTLs on cleaned ITO glass substrates were deposited with SnO_2 and NiO nanoparticle inks at room temperature, respectively, according to previously reported procedure.[35,38] A pinhole free SnO_2 and NiO thin film with uniform tiny nanoparticles were shown in the surface images of scanning electronic microscopy (SEM) and atomic force microscopy (AFM) in Supporting Information Figure S1a−d. The phase images of Figure S1e,f confirm the compactness of these two films. Similarly, two kinds of perovskites, $MAPbI_3$ (MA) and $Cs_{0.05}(FA_{0.85}MA_{0.15})_{0.95}PbBr_{0.15}I_{0.85}$ (CsFAMA), were spin coated on SnO_2/ITO and NiO/ITO substrates, respectively.[32,43] Both kinds of perovskite films show high film crystallinity on those substrates (Figure S2). Excess PbI_2 signal was found in X-ray diffraction patterns of both CsFAMA films.[37] Figure 1 shows the surface morphologies of the perovskite films with high uniformity and compactness. For MA, the grain size of the film on SnO_2 is remarkably larger than that on NiO, which is consistent with other reports.[34,40] That may be attributed to surface wettability variation between NiO and SnO_2. Lower wettability and crystallinity lead to larger grain size of the perovskite film.[33,39,44−46] For CsFAMA, the grain size of both films on NiO and SnO_2 is smaller than that of MA. Moreover, excess PbI_2 flakes turn up in grain boundaries obviously, which is in accordance with our XRD patterns.[38] Each corresponding cross-section scanning electronic microscopy (SEM) image (Figure 1e−h) was shown just below their topography, which also confirms high uniformity in thickness adequately in spite of the resolution limit of our SEM tool. The thicknesses of CsFAMA films on SnO_2/NiO are around 500 and 515 nm, respectively, while those of MA films on SnO_2/NiO are around 390 and 375 nm, respectively.

The UV−vis absorption spectra of each perovskite film were shown in Figure 2a,b. On SnO_2 substrates (Figure 2a), the absorption edge of CsFAMA has a noticeable red shift compared with that of MA on both substrates owing to bandgap shrinkage after alloying Cs and FA ions in the compound, which is verified by the same shift from 772 to 786 nm in their PL spectra, as the red lines show. It is similar for the two kinds of perovskites on NiO substrates (Figure 2b). It is interesting that there also is a slight red shift for both perovskite films when changing the substrates from NiO to SnO_2 (shown in Figure 2), which also is reported by former literature.[31,41]

To test the carrier extraction rate of SnO_2 and NiO films, time-resolved PL (TRPL) was involved to distinguish the difference between SnO_2 and NiO for the two kinds of perovskites. Figure 3a shows the PL of MA quenched by NiO

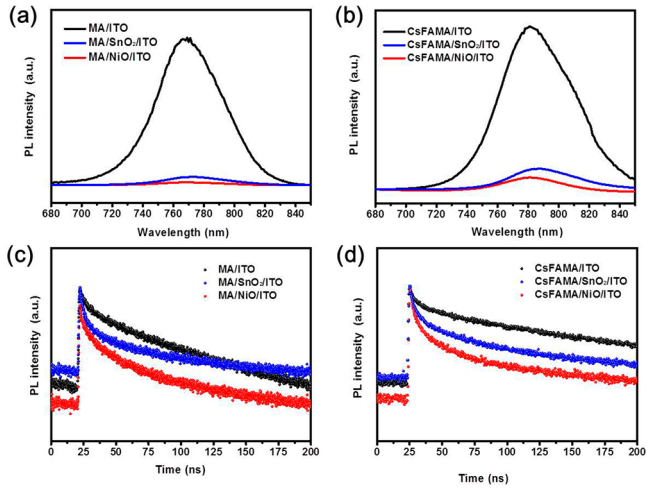

Figure 3. PL spectra of (a) MA perovskite films and (b) CsFAMA perovskite films on ITO, SnO_2/ITO, and NiO/ITO substrates, respectively; TRPL spectra of (c) MA perovskite films and (d) CsFAMA perovskite films on ITO, SnO_2/ITO, and NiO/ITO substrates, respectively.

and SnO_2 in contrast to the control bare ITO substrate, respectively. In comparison, NiO shows stronger carrier extraction ability than SnO_2 although both of them are highly effective, as shown in the quenching extent in Figure 3a,b, which is confirmed by their TRPL results (Figure 3c). For CsFAMA (Figure 3b,d), the PL quenching and TRPL abide by the same law as MA, which further proves the differentia in

DOI: 10.1021/acsaem.8b00687
ACS Appl. Energy Mater. 2018, 1, 3984−3991

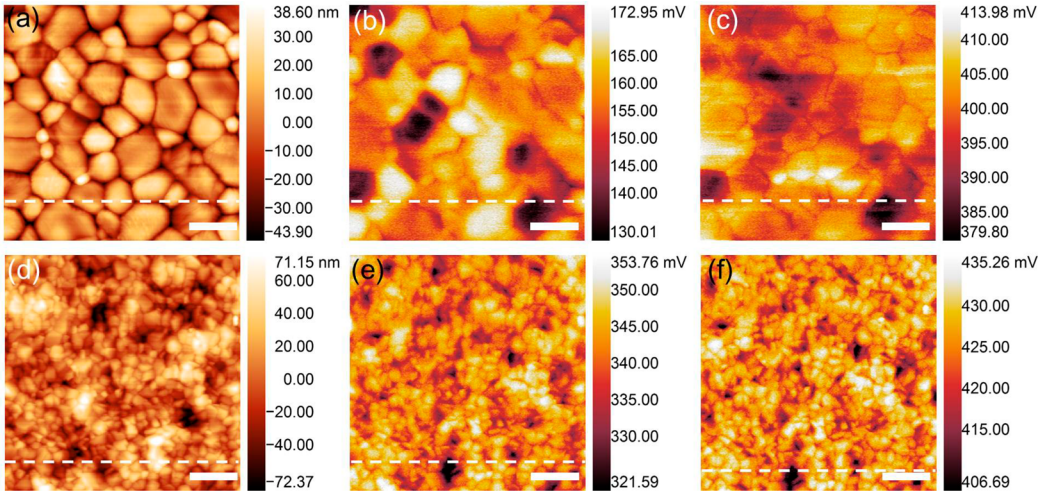

Figure 4. Topographic morphology image (a), dark-SKPM image (b), and light-SKPM image (c) of MA/SnO_2/ITO glass; topographic morphology image (d), dark-SKPM image (e), and light-SKPM image (f) of CsFAMA/SnO_2/ITO glass. The scanning scales are 5 μm × 5 μm, and the scale bars are 1 μm.

carrier extraction ability of them. Regarding the PL decay of each sample, a biexponential decay $I(t) = A_1 \exp(t/\tau_1) + A_2 \exp(t/\tau_2)$ was used to identify the two stage decay time, and the average lifetime can then be determined as $\tau_{av} = (\sum_i A_i\tau_i^2)/(\sum_i A_i\tau_i)$.[47] All the data were summarized in Table S1. The first decay time (τ_1) can reflect the monomolecular recombination driven by defects while the second decay time (τ_2) manifests the irradiative recombination of electron and hole photogenerated in perovskite films as its intrinsic property.[47] Here, the so-called monomolecular recombination can be attributed mainly to electrons or holes only extraction by SnO_2 and NiO, respectively. It is clearly shown that the weight of the first decay increases from near 2% to ca. 7.6% for both SnO_2 and NiO in the system of MA perovskites, which obviously demonstrates the carrier extraction function of them (Table S1). In comparison, NiO's extraction is much faster than that of SnO_2 as τ_1 decreases from 7.78 to 3.79 ns, which demonstrates clearly that the extraction rate of NiO is obviously higher than that of SnO_2 (Table S1). The lifetime of over 100 ns indicates good quality of MA perovskite films while CsFAMA perovskite films also own near 200 ns in lifetime and show excellent quality. Although TRPL can discover the extraction behavior and even compare carrier extraction ability between SnO_2 and NiO, it is still impossible for TRPL to define the extracted carrier type by NiO or SnO_2 although they are deemed already as holes and electrons transport layers, respectively. However, SKPM affords this function exactly.

To eliminate test errors from environment and operation, all the SKPM measurements were conducted with one identical probe at 35% RH and 25 °C within 1 day. A dynamic bucking voltage was used to eliminate the contact potential difference between the tip and the surface when encountering different roughness surfaces.[48−51] Before SKPM tests, topographic AFM measurements were carried out to reveal the surface morphology of each sample. The average roughness of MA/SnO_2/ITO is 16.4 nm while that of CsFAMA/SnO_2/ITO is 23.3 nm shown in Figure 4a,d. The corresponding three-dimensional morphologies are also shown in Figure S3a,b, respectively. For the surface potential image of MA/SnO_2/ITO in the dark (Figure 4b), grain interiors exhibit brightly with slightly black grain boundary lines while the grains vary from each other. The grain size is so large and the film is so compact that it blurs the surface potential difference between grains and grain boundaries, although they are clearly distinguished in the image. The brightness contrast from grain to grain can be attributed in some degree to height difference along with possible difference in the crystallinity of each grain.[7,18,52] As discussed in those literature, the higher the grain crystallinity, the less the nonradiative recombination, faster the extraction rate, and larger the number of electrons or holes left. The final result is the higher brightness. In addition, although the return trace thereotically eliminates the height difference recorded in the first trace described in the working principle of SKPM, the abrupt contrast of grain height definitely inlfuences the recording of contact potential tracing the morphology, which results in the brightness contrast in an alternative way. When light is on, the surface potential map varies except that some deep valleys turn visually dark, as the white dashed line shows (Figure 4c). That seems interesting, and its underlying mechanism remains unclear. The positive surface potential of MA/SnO_2/ITO indicates the possible electron extraction effect of SnO_2 by a depletion region at the interface of MA/SnO_2 in the dark (Figure 4b). The surface potential voltage in the scan region ranges from +130.01 to +172.95 mV in the dark while it is enlarged in its absolute value ranging from from +379.80 to +413.98 mV in the light. The area-mean intensity varies from 155.89 to 398.78 mV by photogenerated electron−hole pairs after illumination (Figure 4c). After illumination, more carriers are generated by photons. The electrons among them will be extracted at the interface of perovskite/SnO_2 by SnO_2, and hence more holes in a balance state remain in the perovskite film and are induced by the SKPM tip. It results in higher absolute values on average than that in the dark. The positive augmentation in surface potential voltage by illumination confirms the electron extraction ability of SnO_2 under the MA perovskite film. The similar phenomenon was also reported on TiO_2 based MA perovskite films,[15,22,53,54] although the values reported varied in different literature even with the same AFM probe, such as Pt/Ir or Au. Whatever, we can attribute these positive values and illumination derived augmentations of surface potential voltages detected by SKPM

DOI: 10.1021/acsaem.8b00687
ACS Appl. Energy Mater. 2018, 1, 3984−3991

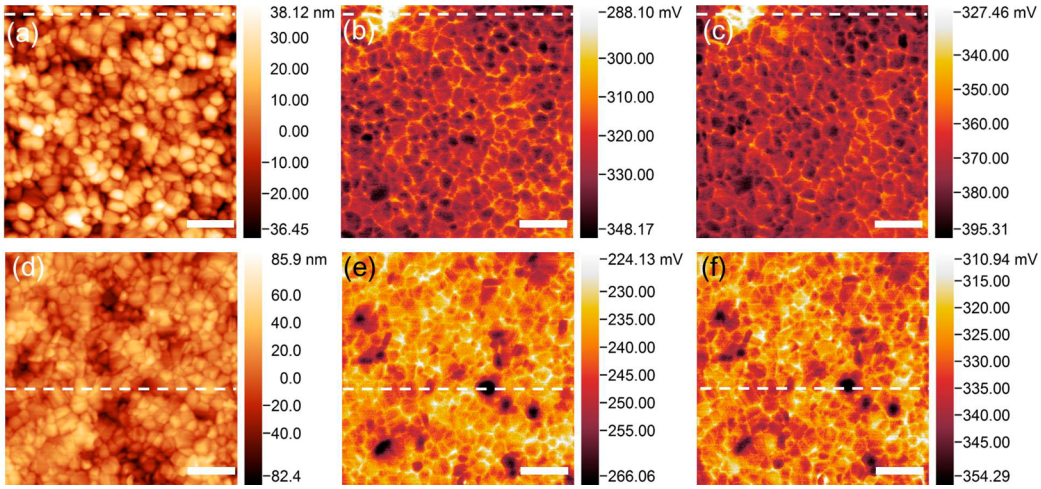

Figure 5. Topographic morphology image (a), dark-SKPM image (b), and light-SKPM image (c) of MA/NiO/ITO glass; topographic morphology image (d), dark-SKPM image (e), and light-SKPM image (f) of CsFAMA/NiO/ITO glass. The scanning scales are 5 μm × 5 μm, and the scale bars are 1 μm.

to the electrons extraction ability of SnO_2. In our work, the function of SnO_2 is also fulfilled in the same way in CsFAMA/SnO_2/ITO (Figure 4e,f). Compared to MA, the grain size of CsFAMA film is much smaller and the roughness is larger, which exhibits a larger contrast in surface potential between grains and grain boundaries. That is more consistent with the phenomena that occurred in perovskite/TiO_2.[23−26] Panels a and c of Figure S4 show the surface potential profiles extracted from the white dashed line shown in Figure 4a−c. Basically in the profile, all the surface potentials both in dark and light follow the height change except for some misfits. The potential contrast between grains and grain boundaries attenuates after illumination. A similar conclusion can be drawn from Figure S4b,d.

In contrast to such an ambiguous explanation of charge separation in perovskites/PEDOT:PSS,[15] this work declares the explicit holes extraction behavior from perovskites to NiO HTLs, examined by SKPM again. Panels a and d of Figure 5 show topographical images of MA and CsFAMA perovskite films deposited on NiO/ITO glass, and the area-mean roughness is around 14.3 and 20.7 nm, respectively. The corresponding three-dimensional surface morphologies were exhibited in Figure S3c,d. Grains and grain boundaries are unambiguous in the surface potential image obtained in the dark (Figure 5b). Different from that of SnO_2, most grain interiors appear darker than grain boundaries, which is attributed to the display habit of the vertical scale bar. In these SKPM images in Figure 5, the darker in color means the higher in absolute value of surface potential voltage. It is clearly shown that the absolute value of surface potential voltage becomes larger after illumination, which demonstrates that new light driven electrons are accumulated at the surface by extracting holes via NiO when the sample is detected by the SKPM probe (Figure 5b,c). This phenomenon has also been detected in the former reports,[53,55,56] where most of the surface potential voltage values became more negative after illumination. However, it is really difficult to determine an accurate dividing span of surface potential voltages to tell which span definitely indexed to a net positive or negative region, because the measured values varied by AFM systems, the work function of SKPM probe materials, and even different synthesis conditions of the samples. In the NiO based devices of our work, for MA perovskite, the surface potential voltage ranged from −288.10 to −348.17 mV in the scan region, which was enlarged in a span (−327.16 to −395.31 mV) after illumination. This phenomenon was also reported in the perovskite devices with PEDOT:PSS as hole transport layer.[53,55] For CsFAMA, the value spans detected in dark and in light are from −224.13 to −266.06 mV and from −310.94 to −354.29 mV, respectively. After illumination, the area-mean surface potential voltage of CsFAMA/NiO/ITO was enhanced obviously from −240.86 to −329.32 mV, where the absolute value augmentation after illumination is also definite. It should be also clarified here that this law stands alone from such features of perovskite films as thickness, grain size, and even morphology, although those factors possibly modify the absolute values within a range, as discussed in some literature.[22,57]

Here, we summarize the surface potential voltages detected by SKPM protocols from both our works and the former reports (Table S1) and draw a firm conclusion that the SnO_2 ETL series lead to the positive augmentation of the surface potential voltage while the NiO HTL series lead to the negative increment of that. Herein, the electron or hole extraction ability of these transport materials is responsible for the positive or negative increment of the surface potential voltage detected by SKPM. Although the surface portential voltage values of the SnO_2 based perovskite devices are obviously positive while those of the NiO based are clearly negative in our work, it is not yet easy to define the accurate dividing span for different AFM systems, different probes and environments, and even objects synthesized by different routes. Beyond any questions, the extracted carrier type can be discriminated by the sign of the increment of the surface potential voltage.

Moreover, the surface potential profiles (Figure S5a,b) extracted from the white dashed lines in Figure 5b,c;e,f also follow the corresponding height traces to a large extent, along with some little discrepancies (Figure S5c,d). The underlying mechanism still needs further exploring. However, regardless of the difference in the images and profiles, the negative surface potential values demonstrate the indisputable holes extraction function of NiO. The area-mean surface potential variation was summarized in Table S2. The actual role of SnO_2 and NiO for

DOI: 10.1021/acsaem.8b00687
ACS Appl. Energy Mater. 2018, 1, 3984−3991

perovskite solar cells can be clearly defined as electron and hole transfer layers by SKPM in this work, respectively.

CONCLUSIONS

In summary, we employed PL and SKPM to identify the type and ability of charge transfer of SnO_2 and NiO for perovskite materials in direct comparison in this work. For both MA and CsFAMA perovskite films, the surface potential voltages of each SnO_2 based device appear positive in the dark while those of NiO based devices appear negative. The absolute surface potential values of both devices were enlarged after illumination. That clearly demonstrates the electrons and holes extraction function of SnO_2 and NiO, respectively. In view of the first decay of TRPL spectra of all the devices, NiO shows an obviously higher carrier extraction rate than SnO_2, neglecting other factors in our work. This work definitely offers us a general and effective method to distinguish the carrier transport ability of either ETLs or HTLs with indisputable defining of carrier types and further to screen out optimal carrier transport materials for perovskite solar cells and more.

ASSOCIATED CONTENT

Supporting Information

The Supporting Information is available free of charge on the ACS Publications website at DOI: 10.1021/acsaem.8b00687.

Supporting figures and tables (PDF)

AUTHOR INFORMATION

Corresponding Authors

*(Z.B.H.) E-mail: hezb@sustc.edu.cn.

*(R.L.) E-mail: phyliurc@cqu.edu.cn.

ORCID

Aleksandra B. Djurišić: 0000-0002-5183-1467

Zhu Bing He: 0000-0002-2775-0894

Author Contributions

‖Y.W. and W.C. contributed equally to this work.

Funding

This work is supported by the National Natural Science Foundation of China (NSFC; Grant No. 61775091), the National Key Research Project MOST (Grant No. 2016YFA0202400), the Natural Science Foundation of the Shenzhen Innovation Committee (Grant No. JCYJ20150529152146471), and the Shenzhen Key Laboratory Project (Grant No. ZDSYS201602261933302).

Notes

The authors declare no competing financial interest.

ACKNOWLEDGMENTS

We thank the Materials Characterization and Preparation Center of SUSTech and the Department of Materials Science and Engineering for the characterizations involved in this work.

ABBREVIATIONS

AFM, atomic force microscopy
CBM, conduction band minimum
CCD, charged couped device
CsFAMA, $(FA_{0.85}MA_{0.15})_{0.95}PbBr_{0.15}I_{0.85}$
DI, deionized
ETLs, eletron transport layers
FAI, Formamidine iodide
HTLs, (hole transport layers)
HTM, hole transport material
MA, $MAPbI_3$ perovskites
MABr, methanaminium bromide
MAI, methanaminium iodide
PCE, power conversion efficiency
PL, photoluminescence
PSCs, perovskite solar cells
SEM, scanning electron microscopy
SKPM, scanning Kelvin probe microscopy
VBM, valence band maximum
XRD, X-ray diffraction

REFERENCES

(1) U.S. National Renewable Energy Laboratory (NREL). *Best Research-Cell Efficiencies*; http://www.nrel.gov/pv/assets/images/efficiency-chart-20180716.jpg.

(2) Ren, Y.-K.; Ding, X.-H.; Wu, Y.-H.; Zhu, J.; Hayat, T.; Alsaedi, A.; Xu, Y.-F.; Li, Z.-Q.; Yang, S.-F.; Dai, S.-Y. Temperature-Assisted Rapid Nucleation: A Facile Method to Optimize the Film Morphology for Perovskite Solar Cells. *J. Mater. Chem. A* **2017**, *5*, 20327−20333.

(3) Ren, Y.-K.; Shi, X.-Q.; Ding, X.-H.; Zhu, J.; Hayat, T.; Alsaedi, A.; Li, Z.-Q.; Xu, X.-X.; Yang, S.-F.; Dai, S.-Y. Facile Fabrication of Perovskite Layers with Large Grains through a Solvent Exchange Approach. *Inorg. Chem. Front.* **2018**, *5*, 348−353.

(4) Kojima, A.; Teshima, K.; Shirai, Y.; Miyasaka, T. Organometal Halide Perovskites as Visible-Light Sensitizers for Photovoltaic Cells. *J. Am. Chem. Soc.* **2009**, *131*, 6050−6051.

(5) Bach, U.; Lupo, D.; Comte, P.; Moser, J. E.; Weissortel, F.; Salbeck, J.; Spreitzer, H.; Gratzel, M. Solid-State Dye-Sensitized Mesoporous Tio2 Solar Cells with High Photon-to-Electron Conversion Efficiencies. *Nature* **1998**, *395*, 583−585.

(6) Peng, J.; Chen, Y.; Zheng, K.; Pullerits, T.; Liang, Z. Insights into Charge Carrier Dynamics in Organo-Metal Halide Perovskites: From Neat Films to Solar Cells. *Chem. Soc. Rev.* **2017**, *46*, 5714−5729.

(7) Hieulle, J.; Stecker, C.; Ohmann, R.; Ono, L. K.; Qi, Y. Scanning Probe Microscopy Applied to Organic−Inorganic Halide Perovskite Materials and Solar Cells. *Small Methods* **2018**, *2*, 1700295.

(8) Wen, Z.; Yeh, M.-H.; Guo, H.; Wang, J.; Zi, Y.; Xu, W.; Deng, J.; Zhu, L.; Wang, X.; Hu, C.; Zhu, L.; Sun, X.; Wang, Z. L. Self-Powered Textile for Wearable Electronics by Hybridizing Fiber-Shaped Nanogenerators, Solar Cells, and Supercapacitors. *Sci. Adv.* **2016**, *2*, No. e1600097.

(9) Zuo, L.; Guo, H.; deQuilettes, D. W.; Jariwala, S.; De Marco, N.; Dong, S.; DeBlock, R.; Ginger, D. S.; Dunn, B.; Wang, M.; Yang, Y. Polymer-Modified Halide Perovskite Films for Efficient and Stable Planar Heterojunction Solar Cells. *Sci. Adv.* **2017**, *3*, No. e1700106.

(10) Bergmann, V. W.; Weber, S. A. L.; Javier Ramos, F.; Nazeeruddin, M. K.; Grätzel, M.; Li, D.; Domanski, A. L.; Lieberwirth, I.; Ahmad, S.; Berger, R. Real-Space Observation of Unbalanced Charge Distribution inside a Perovskite-Sensitized Solar Cell. *Nat. Commun.* **2014**, *5*, 5001.

(11) Melitz, W.; Shen, J.; Kummel, A. C.; Lee, S. Kelvin Probe Force Microscopy and Its Application. *Surf. Sci. Rep.* **2011**, *66*, 1−27.

(12) Jiang, C.-S.; Yang, M.; Zhou, Y.; To, B.; Nanayakkara, S. U.; Luther, J. M.; Zhou, W.; Berry, J. J.; van de Lagemaat, J.; Padture, N. P.; Zhu, K.; Al-Jassim, M. M. Carrier Separation and Transport in Perovskite Solar Cells Studied by Nanometre-Scale Profiling of Electrical Potential. *Nat. Commun.* **2015**, *6*, 8397.

(13) Dymshits, A.; Henning, A.; Segev, G.; Rosenwaks, Y.; Etgar, L. The Electronic Structure of Metal Oxide/Organo Metal Halide Perovskite Junctions in Perovskite Based Solar Cells. *Sci. Rep.* **2015**, *5*, 8704.

(14) Guerrero, A.; Juarez-Perez, E. J.; Bisquert, J.; Mora-Sero, I.; Garcia-Belmonte, G. Electrical Field Profile and Doping in Planar Lead Halide Perovskite Solar Cells. *Appl. Phys. Lett.* **2014**, *105*, 133902.

DOI: 10.1021/acsaem.8b00687
ACS Appl. Energy Mater. 2018, 1, 3984−3991

(15) Yun, J. S.; Ho-Baillie, A.; Huang, S.; Woo, S. H.; Heo, Y.; Seidel, J.; Huang, F.; Cheng, Y.-B.; Green, M. A. Benefit of Grain Boundaries in Organic−Inorganic Halide Planar Perovskite Solar Cells. *J. Phys. Chem. Lett.* **2015**, *6*, 875−880.
(16) Yun, J. S.; Seidel, J.; Kim, J.; Soufiani, A. M.; Huang, S.; Lau, J.; Jeon, N. J.; Seok, S. I.; Green, M. A.; Ho-Baillie, A. Critical Role of Grain Boundaries for Ion Migration in Formamidinium and Methylammonium Lead Halide Perovskite Solar Cells. *Adv. Energy Mater.* **2016**, *6*, 1600330.
(17) Huang, J.; Yuan, Y.; Shao, Y.; Yan, Y. Understanding the Physical Properties of Hybrid Perovskites for Photovoltaic Applications. *Nat.Rev. Mater.* **2017**, *2*, 17042.
(18) Shao, Y.; Fang, Y.; Li, T.; Wang, Q.; Dong, Q.; Deng, Y.; Yuan, Y.; Wei, H.; Wang, M.; Gruverman, A.; Shield, J.; Huang, J. Grain Boundary Dominated Ion Migration in Polycrystalline Organic-Inorganic Halide Perovskite Films. *Energy Environ. Sci.* **2016**, *9*, 1752−1759.
(19) Ravishankar, S.; Gharibzadeh, S.; Roldán-Carmona, C.; Grancini, G.; Lee, Y.; Ralaiarisoa, M.; Asiri, A. M.; Koch, N.; Bisquert, J.; Nazeeruddin, M. K. Influence of Charge Transport Layers on Open-Circuit Voltage and Hysteresis in Perovskite Solar Cells. *Joule* **2018**, *2*, 788−798.
(20) Cai, M.; Ishida, N.; Li, X.; Yang, X.; Noda, T.; Wu, Y.; Xie, F.; Naito, H.; Fujita, D.; Han, L. Control of Electrical Potential Distribution for High-Performance Perovskite Solar Cells. *Joule* **2018**, *2*, 296−306.
(21) Xu, G.; Xue, R.; Chen, W.; Zhang, J.; Zhang, M.; Chen, H.; Cui, C.; Li, H.; Li, Y.; Li, Y. New Strategy for Two-Step Sequential Deposition: Incorporation of Hydrophilic Fullerene in Second Precursor for High-Performance P-I-N Planar Perovskite Solar Cells. *Adv. Energy Mater.* **2018**, *8*, 1703054.
(22) Zhao, Z.; Chen, X.; Wu, H.; Wu, X.; Cao, G. Probing the Photovoltage and Photocurrent in Perovskite Solar Cells with Nanoscale Resolution. *Adv. Funct. Mater.* **2016**, *26*, 3048−3058.
(23) Kim, Y. C.; Jeon, N. J.; Noh, J. H.; Yang, W. S.; Seo, J.; Yun, J. S.; Ho-Baillie, A.; Huang, S.; Green, M. A.; Seidel, J.; Ahn, T. K.; Seok, S. I. Beneficial Effects of Pbi2 Incorporated in Organo-Lead Halide Perovskite Solar Cells. *Adv. Energy Mater.* **2016**, *6*, 1502104.
(24) Chen, Q.; Zhou, H.; Song, T.-B.; Luo, S.; Hong, Z.; Duan, H.-S.; Dou, L.; Liu, Y.; Yang, Y. Controllable Self-Induced Passivation of Hybrid Lead Iodide Perovskites toward High Performance Solar Cells. *Nano Lett.* **2014**, *14*, 4158−4163.
(25) Salado, M.; Kokal, R. K.; Calio, L.; Kazim, S.; Deepa, M.; Ahmad, S. Identifying the Charge Generation Dynamics in Cs+-Based Triple Cation Mixed Perovskite Solar Cells. *Phys. Chem. Chem. Phys.* **2017**, *19*, 22905−22914.
(26) Zhang, M.; Yun, J. S.; Ma, Q.; Zheng, J.; Lau, C. F. J.; Deng, X.; Kim, J.; Kim, D.; Seidel, J.; Green, M. A.; Huang, S.; Ho-Baillie, A. W. Y. High-Efficiency Rubidium-Incorporated Perovskite Solar Cells by Gas Quenching. *ACS Energy Lett.* **2017**, *2*, 438−444.
(27) Garrett, J. L.; Tennyson, E. M.; Hu, M.; Huang, J.; Munday, J. N.; Leite, M. S. Real-Time Nanoscale Open-Circuit Voltage Dynamics of Perovskite Solar Cells. *Nano Lett.* **2017**, *17*, 2554−2560.
(28) Haque, M. A.; Sheikh, A. D.; Guan, X. W.; Wu, T. Metal Oxides as Efficient Charge Transporters in Perovskite Solar Cells. *Adv. Energy Mater.* **2017**, *7*, 1602803.
(29) Cho, A. N.; Park, N. G. Impact of Interfacial Layers in Perovskite Solar Cells. *ChemSusChem* **2017**, *10*, 3687−3704.
(30) Kim, H.; Lim, K. G.; Lee, T. W. Planar Heterojunction Organometal Halide Perovskite Solar Cells: Roles of Interfacial Layers. *Energy Environ. Sci.* **2016**, *9*, 12−30.
(31) Chen, W.; Liu, F.-Z.; Feng, X.-Y.; Djurišić, A. B.; Chan, W. K.; He, Z.-B. Cesium Doped Niox as an Efficient Hole Extraction Layer for Inverted Planar Perovskite Solar Cells. *Adv. Energy Mater.* **2017**, *7*, 1700722.
(32) Chen, W.; Xu, L.; Feng, X.; Jie, J.; He, Z. Metal Acetylacetonate Series in Interface Engineering for Full Low-Temperature-Processed, High-Performance, and Stable Planar Perovskite Solar Cells with Conversion Efficiency over 16% on 1 Cm2 Scale. *Adv. Mater.* **2017**, *29*, 1603923.
(33) You, J.; Meng, L.; Song, T.-B.; Guo, T.-F.; Yang, Y.; Chang, W.-H.; Hong, Z.; Chen, H.; Zhou, H.; Chen, Q.; Liu, Y.; De Marco, N.; Yang, Y. Improved Air Stability of Perovskite Solar Cells Via Solution-Processed Metal Oxide Transport Layers. *Nat. Nanotechnol.* **2015**, *11*, 75.
(34) Nie, W.; Tsai, H.; Blancon, J.-C.; Liu, F.; Stoumpos, C. C.; Traore, B.; Kepenekian, M.; Durand, O.; Katan, C.; Tretiak, S.; Crochet, J.; Ajayan, P. M.; Kanatzidis, M.; Even, J.; Mohite, A. D. Critical Role of Interface and Crystallinity on the Performance and Photostability of Perovskite Solar Cell on Nickel Oxide. *Adv. Mater.* **2018**, *30*, 1703879.
(35) Chen, W.; Zhang, G.-n.; Xu, L.-m.; Gu, R.; Xu, Z.-h.; Wang, H.-j.; He, Z.-b. Low Temperature Processed, High-Performance and Stable Niox Based Inverted Planar Perovskite Solar Cells Via a Poly(2-Ethyl-2-Oxazoline) Nanodots Cathode Electron-Extraction Layer. Mater. *Today Energy* **2016**, *1−2*, 1−10.
(36) Ren, X.; Yang, D.; Yang, Z.; Feng, J.; Zhu, X.; Niu, J.; Liu, Y.; Zhao, W.; Liu, S. F. Solution-Processed Nb:Sno2 Electron Transport Layer for Efficient Planar Perovskite Solar Cells. *ACS Appl. Mater. Interfaces* **2017**, *9*, 2421−2429.
(37) Jiang, Q.; Zhang, L.; Wang, H.; Yang, X.; Meng, J.; Liu, H.; Yin, Z.; Wu, J.; Zhang, X.; You, J. Enhanced Electron Extraction Using SnO2 for High-Efficiency Planar-Structure HC(NH2)2PbI3-Based Perovskite Solar Cells. *Nat. Energy* **2016**, *2*, 16177.
(38) Jiang, Q.; Chu, Z.; Wang, P.; Yang, X.; Liu, H.; Wang, Y.; Yin, Z.; Wu, J.; Zhang, X.; You, J. Planar-Structure Perovskite Solar Cells with Efficiency Beyond 21%. *Adv. Mater.* **2017**, *29*, 1703852.
(39) Ke, W.; Fang, G.; Liu, Q.; Xiong, L.; Qin, P.; Tao, H.; Wang, J.; Lei, H.; Li, B.; Wan, J.; Yang, G.; Yan, Y. Low-Temperature Solution-Processed Tin Oxide as an Alternative Electron Transporting Layer for Efficient Perovskite Solar Cells. *J. Am. Chem. Soc.* **2015**, *137*, 6730−6733.
(40) Yang, G.; Wang, C. L.; Lei, H. W.; Zheng, X. L.; Qin, P. L.; Xiong, L. B.; Zhao, X. Z.; Yan, Y. F.; Fang, G. J. Interface Engineering in Planar Perovskite Solar Cells: Energy Level Alignment, Perovskite Morphology Control and High Performance Achievement. *J. Mater. Chem. A* **2017**, *5*, 1658−1666.
(41) Xie, J.; Huang, K.; Yu, X.; Yang, Z.; Xiao, K.; Qiang, Y.; Zhu, X.; Xu, L.; Wang, P.; Cui, C.; Yang, D. Enhanced Electronic Properties of Sno2 Via Electron Transfer from Graphene Quantum Dots for Efficient Perovskite Solar Cells. *ACS Nano* **2017**, *11*, 9176−9182.
(42) Chen, W.; Zhou, Y.; Wang, L.; Wu, Y.; Tu, B.; Yu, B.; Liu, F.; Tam, H. W.; Wang, G.; Djurišić, A. B.; Huang, L.; He, Z. Molecule-Doped Nickel Oxide: Verified Charge Transfer and Planar Inverted Mixed Cation Perovskite Solar Cell. *Adv. Mater.* **2018**, *30*, 1800515.
(43) Habisreutinger, S. N.; Wenger, B.; Snaith, H. J.; Nicholas, R. J. Dopant-Free Planar N−I−P Perovskite Solar Cells with Steady-State Efficiencies Exceeding 18%. *ACS Energy Lett.* **2017**, *2*, 622−628.
(44) Yu, H.; Ryu, J.; Lee, J. W.; Roh, J.; Lee, K.; Yun, J.; Lee, J.; Kim, Y. K.; Hwang, D.; Kang, J.; Kim, S. K.; Jang, J. Large Grain-Based Hole-Blocking Layer-Free Planar-Type Perovskite Solar Cell with Best Efficiency of 18.20%. *ACS Appl. Mater. Interfaces* **2017**, *9*, 8113−8120.
(45) Sung, H.; Ahn, N.; Jang, M. S.; Lee, J.-K.; Yoon, H.; Park, N.-G.; Choi, M. Transparent Conductive Oxide-Free Graphene-Based Perovskite Solar Cells with over 17% Efficiency. *Adv. Energy Mater.* **2016**, *6*, 1501873.
(46) Nie, W. Y.; Tsai, H. H.; Asadpour, R.; Blancon, J. C.; Neukirch, A. J.; Gupta, G.; Crochet, J. J.; Chhowalla, M.; Tretiak, S.; Alam, M. A.; Wang, H. L.; Mohite, A. D. High-Efficiency Solution-Processed Perovskite Solar Cells with Millimeter-Scale Grains. *Science* **2015**, *347*, 522−525.
(47) Feng, X.; Su, H.; Wu, Y.; Wu, H.; Xie, J.; Liu, X.; Fan, J.; Dai, J.-F.; He, Z. Photon-Generated Carriers Excited Superoxide Species Inducing Long-Term Photoluminescence Enhancement of Mapbi3 Perovskite Single Crystals. *J. Mater. Chem. A* **2017**, *5*, 12048−12053.

DOI: 10.1021/acsaem.8b00687
ACS Appl. Energy Mater. 2018, 1, 3984−3991

(48) Nonnenmacher, M.; O'Boyle, M. P.; Wickramasinghe, H. K. Kelvin Probe Force Microscopy. *Appl. Phys. Lett.* **1991**, *58*, 2921−2923.
(49) Nonnenmacher, M.; O'Boyle, M.; Wickramasinghe, H. K. Surface Investigations with a Kelvin Probe Force Microscope. *Ultramicroscopy* **1992**, *42-44*, 268−273.
(50) Lin, S.-q.; Shao, T.-m. Charge Erasure Analysis on the Nanoscale Using Kelvin Probe Force Microscopy. *AIP Adv.* **2017**, *7*, 075104.
(51) Moores, B.; Hane, F.; Eng, L.; Leonenko, Z. Kelvin Probe Force Microscopy in Application to Biomolecular Films: Frequency Modulation, Amplitude Modulation, and Lift Mode. *Ultramicroscopy* **2010**, *110*, 708−711.
(52) Rothmann, M. U.; Li, W.; Etheridge, J.; Cheng, Y.-B. Microstructural Characterisations of Perovskite Solar Cells − from Grains to Interfaces: Techniques, Features, and Challenges. *Adv. Energy Mater.* **2017**, *7*, 1700912.
(53) Li, J.-J.; Ma, J.-Y.; Ge, Q.-Q.; Hu, J.-S.; Wang, D.; Wan, L.-J. Microscopic Investigation of Grain Boundaries in Organolead Halide Perovskite Solar Cells. *ACS Appl. Mater. Interfaces* **2015**, *7*, 28518−28523.
(54) Li, J.-J.; Ma, J.-Y.; Hu, J.-S.; Wang, D.; Wan, L.-J. Influence of N,N-Dimethylformamide Annealing on the Local Electrical Properties of Organometal Halide Perovskite Solar Cells: An Atomic Force Microscopy Investigation. *ACS Appl. Mater. Interfaces* **2016**, *8*, 26002−26007.
(55) Chang, J.; Zhu, H.; Xiao, J.; Isikgor, F. H.; Lin, Z.; Hao, Y.; Zeng, K.; Xu, Q.-H.; Ouyang, J. Enhancing the Planar Heterojunction Perovskite Solar Cell Performance through Tuning the Precursor Ratio. *J. Mater. Chem. A* **2016**, *4*, 7943−7949.
(56) Chiesa, M.; Burgi, L.; Kim, J. S.; Shikler, R.; Friend, R. H.; Sirringhaus, H. Correlation between Surface Photovoltage and Blend Morphology in Polyfluorene-Based Photodiodes. *Nano Lett.* **2005**, *5*, 559−563.
(57) Adhikari, N.; Dubey, A.; Khatiwada, D.; Mitul, A. F.; Wang, Q.; Venkatesan, S.; Iefanova, A.; Zai, J.; Qian, X.; Kumar, M.; Qiao, Q. Interfacial Study to Suppress Charge Carrier Recombination for High Efficiency Perovskite Solar Cells. *ACS Appl. Mater. Interfaces* **2015**, *7*, 26445−26454.

DOI: 10.1021/acsaem.8b00687
ACS Appl. Energy Mater. 2018, 1, 3984−3991